

# Generative Design of Crystal Structures by Point Cloud Representations and Diffusion Model

## Author Information

---

### Affiliations



School of Physics and Electronic Engineering, Jiangsu University, Zhenjiang, Jiangsu 212013, PR China

Jiangsu Engineering Research Center on Quantum Perception and Intelligent Detection of Agricultural Information, Zhenjiang, 212013, China

Zhelin Li (<https://orcid.org/0009-0000-7050-312X>), Rami Mrad (<https://orcid.org/0009-0002-8350-0141>), Runxian Jiao (<https://orcid.org/0009-0006-3852-6739>), Guan Huang, Jun Shan, Shibing Chu & Yuanping Chen

### Contributions

Z.L.: conceptualization, method, software, investigation, formal analysis, model validation, writing original draft; R.M: editing, model validation and investigation; R.J, G.H and J.S: DFT calculation guide; S.C and Y.C: conceptualization, writing review, funding acquisition, resources and supervision.

### Corresponding author

Correspondence to: Shibing Chu (<https://orcid.org/0009-0000-8909-1786>), Yuanping Chen (<https://orcid.org/0000-0001-5349-3484>)

### Abstract

---

Efficiently generating energetically stable crystal structures has long been a challenge in

material design, primarily due to the immense arrangement of atoms in a crystal lattice. To facilitate the discovery of stable materials, we present a framework for the generation of synthesizable materials leveraging a point cloud representation to encode intricate structural information. At the heart of this framework lies the introduction of a diffusion model as its foundational pillar. To gauge the efficacy of our approach, we employed it to reconstruct input structures from our training datasets, rigorously validating its high reconstruction performance. Furthermore, we demonstrate the profound potential of point cloud-based crystal diffusion (PCCD) by generating entirely new materials, emphasizing their synthesizability. Our research stands as a noteworthy contribution to the advancement of materials design and synthesis through the cutting-edge avenue of generative design instead of conventional substitution or experience-based discovery.

## Introduction

---

The continuous advancement of technology hinges significantly on the development of new materials, making it essential to unravel the complex relationships between molecular or crystal structures and their properties. Currently, two main methods are used for designing crystal structures: altering existing materials using scientific intuition and empirical principles or global optimization algorithms<sup>1</sup> and mining material databases with the Materials Project (MP)<sup>2</sup>, known as high-throughput virtual screening<sup>3</sup>, which has shown great success in various applications. However, the computational expense associated with density functional theory (DFT) calculations renders an exhaustive search of the theoretical material space infeasible<sup>4</sup>. In recent years, there has been a notable surge in research dedicated to harnessing artificial intelligence for the exploration of new materials<sup>5, 6, 7, 8, 9, 10</sup>. However, within the field of

crystallography, the predominant application of ML techniques is focused on predicting material properties, such as composition, band gap, or formation energy<sup>11, 12, 13</sup>. Consequently, the utilization of ML algorithms for crystal generation remains relatively nascent, underscoring the pressing need for the further development of artificial intelligence-generated content (AIGC) within the realm of crystallography.

In the field of material exploration, generative models have been proven to be particularly effective<sup>7</sup>. Over the past few years, two fundamental models have been widely applied: the generative adversarial network (GAN)<sup>14</sup> and the variational autoencoder (VAE)<sup>15</sup>. Currently, an array of studies has been dedicated to structure generation, drawing on the capabilities of these two models. An example is the study conducted by Jordan Hoffmann *et al.*<sup>16</sup>, in which voxel representation was employed for crystals, a VAE was utilized for voxel data generation, and a U-Net model was subsequently applied for voxel classification. Zekun Ren *et al.*<sup>5</sup> employed VAE for the reverse design of materials. Kim *et al.*<sup>7</sup> utilized a GAN model to explore structures within the Mg-Mn-O ternary system, while Baekjun Kim *et al.*<sup>8</sup> employed a Wasserstein generative adversarial network (WGAN) in their quest to discover crystalline porous materials. These research endeavors highlight the versatility and promise of generative models in the context of material discovery and design.

Nevertheless, most models address the challenge of how to improve the quality of generation results<sup>17</sup>. Jonathan Ho *et al.*<sup>18</sup> introduced a novel generative model known as the denoising diffusion probabilistic model (DDPM). Notably, various research teams, such as OpenAI<sup>19, 20</sup>, NVIDIA<sup>21</sup> and Google<sup>22</sup>, have achieved significant breakthroughs in the

application<sup>23</sup> of this model. Considering its excellent generative capability, we aim to investigate the latent potential of this model in the domain of structure generation and its potential to enhance the creative aspects of the model. Additionally, to minimize computational expenses and tailor diffusion modeling, we propose a point cloud representation<sup>24</sup> to encode atom sites, element information, and lattice constants.

In this paper, we introduce a streamlined deep learning framework for crystal generation: point cloud-based crystal diffusion (PCCD). To test the model's reliability, we intentionally added noise to our dataset and then used the PCCD to reconstruct the majority of the inputs with only minor deviations. Furthermore, we calculated the energy above hull ( $E_{\text{hull}}$ ) per atom for a set of crystal structures generated by PCCD, revealing that many of these structures had low energy values, indicating their potential significance. Furthermore, our analysis revealed structures not in the database or with a stable phonon structure, emphasizing the ability of PCCD to generate new and potentially significant crystal structures.

## Results

---

In the PCCD, the training of the diffusion model involves the incremental addition of noise, with the model essentially learning how this noise is incorporated into the data. In an ideal scenario, saving the data from the training set, along with the added noise, should enable the eventual reconstruction of these data. To validate the model's effectiveness, we experimented by introducing noise to randomly selected data points from the training dataset, after which the resultant data were retained. These noise-augmented data served as the initial random inputs for the subsequent generation process. Setting our approach apart is the establishment of a direct

one-to-one correspondence between the generated outcomes and the expected matches within the database. We then compared the restored data to the original dataset, as illustrated in Fig. 1, providing a robust assessment of the model's reconstruction performance. This experiment serves as a rigorous validation of the model's capabilities.

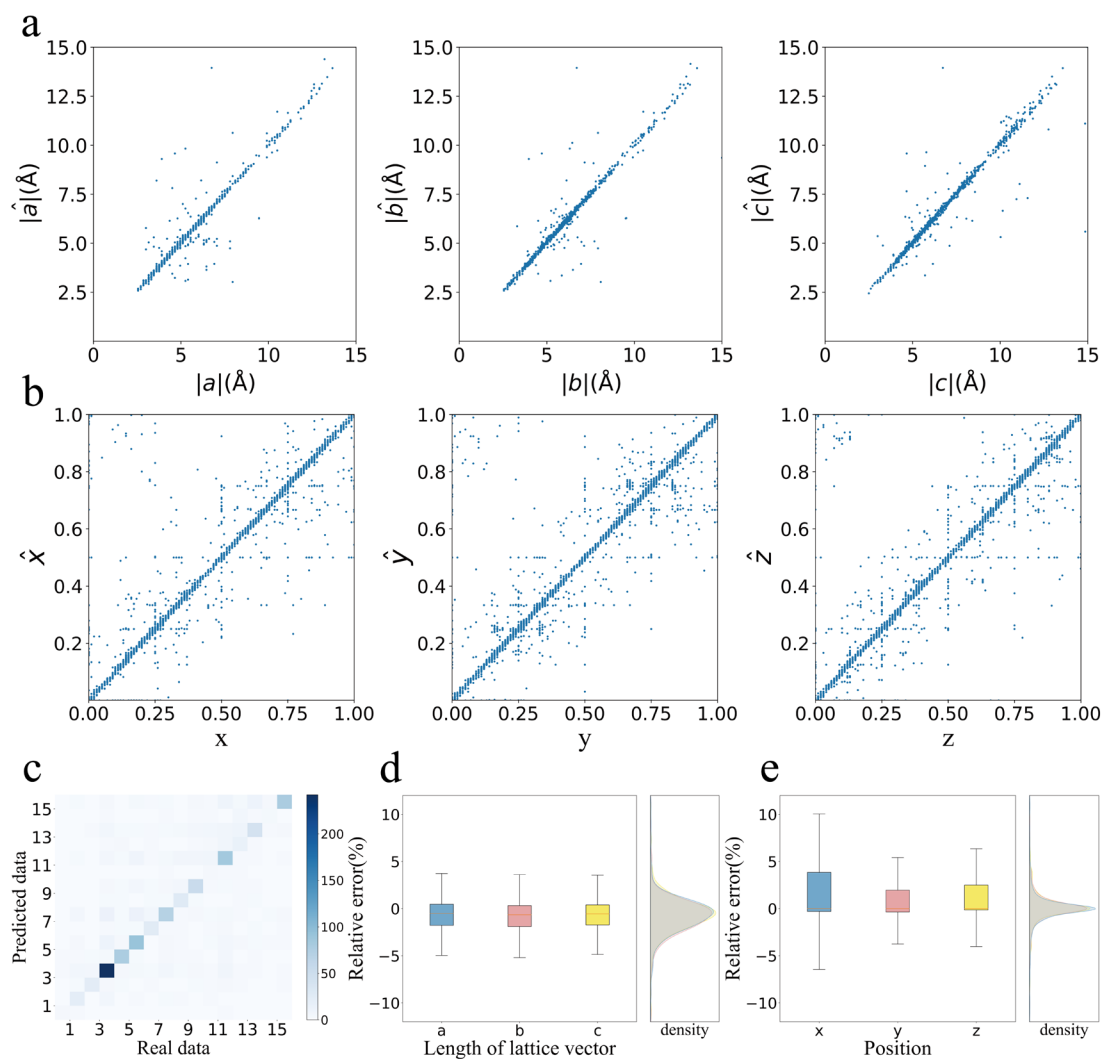


**Fig. 1|Reconstruction results of the PCCD. a.** The parity plots for lattice lengths of generated materials and original materials. **b.** The parity plots for the atomic positions of the generated materials and original materials. **c.** Heatmap of the atom number relationship between the generated materials and original materials. **d.** Box plot of the lattice length relative error with density distribution. **e.** Box plot of the relative errors of the atomic x, y, and z coordinates with density distribution.

respect to the density distribution.

Given that we did not specify the number of atoms in the PCCD, the accuracy of predicting the atom count serves as a direct indicator of the model's performance. In Fig. 1c, a heatmap illustrates the relationship between the sum of atoms in the original data and the data predicted by the PCCD. Notably, a clear diagonal line represents accurate predictions, and the accuracy rate is 67.81% (868 out of 1280 samples). Among these 868 samples with accurately predicted atom counts, we further calculated the relative errors for the lattice length of each corresponding atom, where  $|\mathbf{a}|$ ,  $|\mathbf{b}|$ ,  $|\mathbf{c}|$  are the original lattice lengths and  $|\hat{\mathbf{a}}|$ ,  $|\hat{\mathbf{b}}|$ ,  $|\hat{\mathbf{c}}|$  are the predicted lattice lengths (as shown in Fig. 1a) and their coordinates (depicted in Fig. 1b). A significant portion of these errors is visibly clustered around the  $y = x$  line. To gain deeper insights into their distribution, we conducted a detailed analysis using box plots for both aspects, as presented in Fig. 1d and Fig. 1e. Fig. 1d displays the box plot for the relative errors of the lattice parameters  $a$ ,  $b$ , and  $c$ . The acceptable ranges for  $a$ ,  $b$ , and  $c$  typically fall within upper limits of 3.81%, 3.66%, and 3.57%, respectively, and lower limits of -5.12%, -5.23%, and -4.90%, respectively. The effective rates for these parameters are as follows: 88.48% for lattice parameters  $a$ , 90.55% for lattice parameters  $b$ , and 89.40% for lattice parameters  $c$ . Alongside the box plots, the kernel density function plots help illustrate the concentration of the data. In Fig. 1e, we present the box plot for the relative errors of the  $x$ ,  $y$ , and  $z$  coordinates for each atom. The typical acceptable ranges for  $x$ ,  $y$ , and  $z$  coordinates fall within the upper limits of 10.05%, 5.44%, and 6.44%, respectively, and lower limits of -6.50%, -3.84%, and -4.09%, respectively. The effective rates for these coordinates are calculated as 70.83% for  $x$ , 71.60% for  $y$ , and 72.02% for  $z$ . Most of the errors are relatively small, and they can be readily corrected during DFT

geometry optimization. This analysis indicates that the framework is already functional and effective. However, we also conducted a more in-depth analysis to explore the objective factors that may influence model errors.

	<i>a</i>	<i>b</i>	<i>c</i>	<i>x</i>	<i>y</i>	<i>z</i>
Efficiency	88.48%	90.55%	89.40%	70.83%	71.60%	72.02%
Upper limits	3.81%	3.66%	3.57%	10.05%	5.44%	6.44%
Lower limits	-5.12%	-5.23%	-4.90%	-6.50%	-3.84%	-4.09%

**Table 1|Data details for Fig. 1.** Efficiency calculations according to the box plots in Fig. 1d and Fig. 1e. The upper and lower limits are shown for the box plots in Fig. 1d and Fig. 1e, respectively.

A significant contributing factor to the performance limitations of PCCD lies in the preprocessing stage before training. To facilitate the normalization of lattice vectors and enhance reversibility, all lattice vector data (data in the 3rd channel) were divided by 15. Consequently, the model's capacity was restricted to generating values within the range of -1 to 1, which, in turn, led to a limitation in predicting lattice vectors. Specifically, the model could predict only lattice vectors with a maximum length of 15 Å. As a consequence, structures featuring lattice vectors exceeding the maximum could not be accurately predicted. Upon calculating the relative errors for the lattice lengths of each atom across all samples (a total of 1280), we observed less favorable outcomes due to this limitation. The box plots vividly illustrate that the effective rates for lattice vector length were only 73.98% for the ‘*a*’ lattice

parameter, 75.39% for 'b', and 71.64% for 'c'. This highlights the significant correspondence between the errors in both the atom counts and lattice vector length predictions.

Notably, many of these errors were associated with structures featuring at least one lattice vector longer than the maximum. This suggests a substantial interrelation between the atom count and lattice vector predictions, despite their presence in different data channels. Furthermore, the comparison of the  $x$ ,  $y$  and  $z$  positions of atoms, as shown in the three figures in Fig. 1b, reveals that a portion of the data clustered around the position (0,1). These data points were excluded when calculating statistics, as they were considered erroneous. However, it is important to note that crystal cells are periodic, and such data points are essentially equivalent to (0,0) or (1,1). This periodicity factor contributes to lower accuracy in the statistical analysis.

In comparison to models tailored for specific material components, such as the Mg-Mn-O or  $V_xO_y$  systems<sup>7, 25</sup>, PCCD demonstrates superior generalization capabilities. This means that we can effectively generate crystal structures composed of any combination of elements, provided that the total number of elements does not exceed three. As depicted in Fig. 2, PCCD enables the generation of unary systems (Fig. 2a), binary systems (Fig. 2b), and ternary systems (Fig. 2c), demonstrating its versatility and broad applicability. These findings also prove the



diversity of this framework (Fig. 2d, Fig. 2e and Fig. 2f).

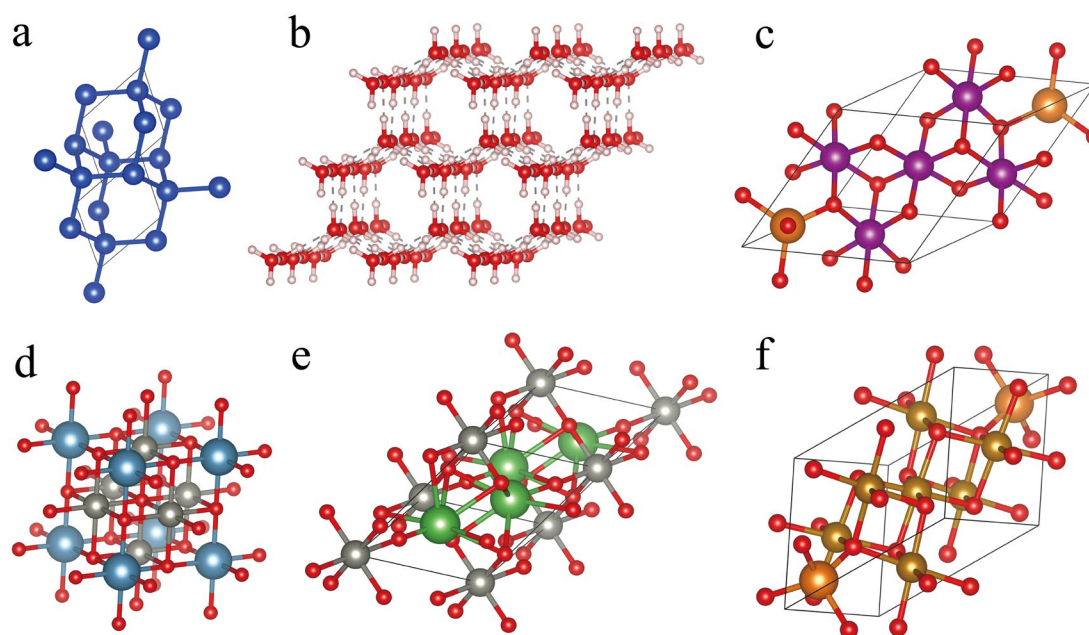


**Fig. 2|Examples of generated crystals. a.** Sample of the predicted data Si system. **b.** A sample of the predicted data  $3 \times 3$  supercell for the H-O system (H<sub>2</sub>O). **c.** Predicted data of the unit cell for the Mg-Mn-O system (Mg<sub>2</sub>Mn<sub>3</sub>O<sub>8</sub>). **d.** Unit cell generated for CaZn<sub>3</sub>O<sub>4</sub>. **e.** Unit cell generated for La<sub>2</sub>ZnO<sub>4</sub>. **f.** Unit cell generated for MgFe<sub>2</sub>O<sub>4</sub>.

We generated a batch of structures that consisted of rare earth elements, alkaline earth elements, transition metal elements, and oxygen. Following an initial screening process, we identified 746 structures without relaxation. We employed the Vienna Ab Initio Simulation Package (VASP)<sup>26, 27</sup> to calculate the total energy. The generalized gradient approximation (GGA)<sup>28</sup> given by the Perdew–Burke–Ernzerhof (PBE) parametrization<sup>29</sup> was used to describe exchange–correlation interactions. Furthermore, we utilized the *pymatgen* package to calculate the  $E_{\text{hull}}$  per atom<sup>30</sup> and found that approximately 62.68% of the structures exhibited values less than 0.25 eV/atom (Fig. 3). In comparison, according to Yong Zhao’s PGCGM<sup>4</sup>, out of 1579 structures, 106 had values less than 0.25 eV/atom (5.3%). Sungwon Kim’s model<sup>7</sup> and Juhwan

Noh's model, known as iMatGen<sup>25</sup>, are two earlier models that have also made significant contributions to the field of GAN and VAE. Both of these authors assert that a structure with an  $E_{\text{hull}}$  less than 80 meV/atom can be considered relatively stable. In their respective paper, Sungwon Kim's work obtained 113 results with an  $E_{\text{hull}}$  per atom less than 80 meV/atom from 6000 generated structures, while iMatGen achieved 40 such results from 10,981 structures, with a ratio of 1.8% and 0.36%, respectively. In contrast, we identified 122 structures that met these criteria from a pool of 746 generated structures (16.35%). Further details can be found in the Supplementary Information. These findings suggest that the diffusion model may, to some extent, outperform GANs or VAEs in this field. It is worth highlighting that despite being a simplified version designed to explore the potential of the diffusion model and point cloud usage in the field of materials, our framework, akin to a pretrained model, has demonstrated comparable or even superior effectiveness in various aspects when compared to many other existing models.

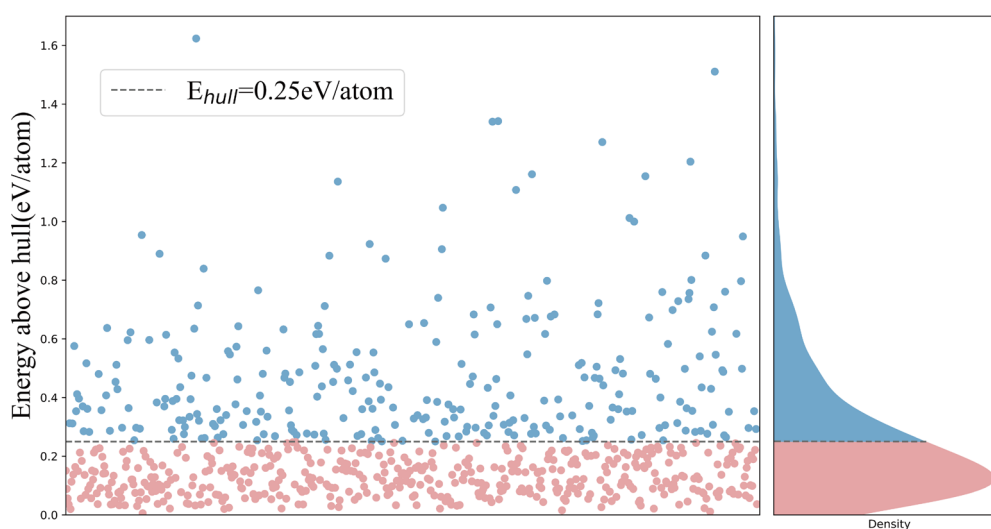


**Fig. 3|**The distribution of  $E_{\text{hull}}$  per atom for the generated data (746 materials). The red part shows that the structures exhibit energies less than  $E_{\text{hull}}=0.25$  eV/atom, while the structures that exceed  $E_{\text{hull}}=0.25$  eV/atom are marked by blue points.

Moreover, we chose three materials ( $\text{Ca}_2\text{SnO}_4$ ,  $\text{Mg}_3\text{CdO}_4$ , and  $\text{MgSc}_2\text{O}_4$ ) from the pool of 746 previously generated structures for further investigation. We utilized DS-PAW<sup>31</sup> for structural relaxation calculations and band structure assessments. Importantly, all three materials were successfully optimized and exhibited nonzero bandgaps, confirming their stability via DFT validation. Subsequently, we conducted phonon spectrum calculations for these selected materials (as shown in Fig. 4), and all the materials demonstrated structural stability.

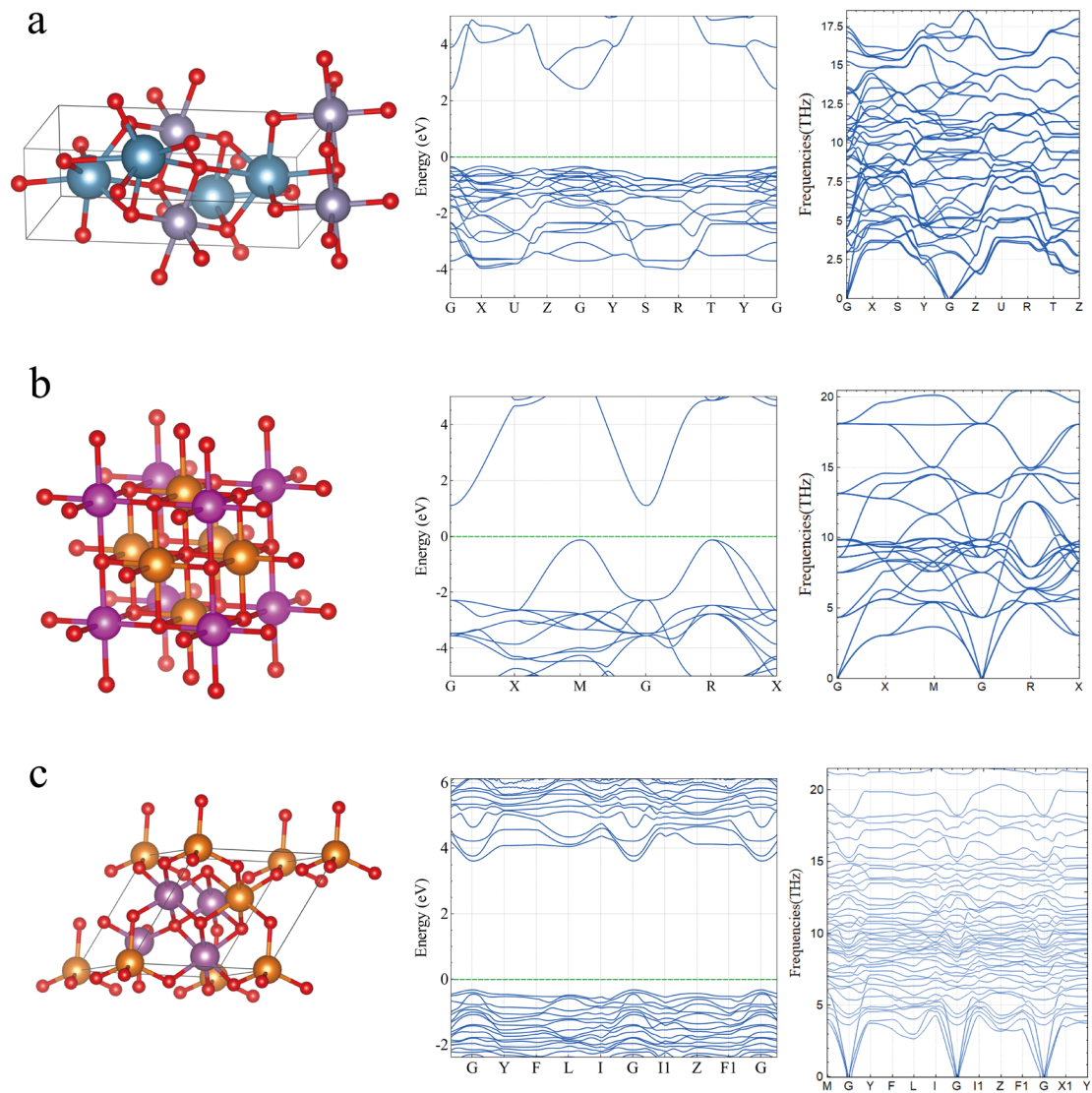


Fig. 4|Graphical depiction of the structures and their DFT calculations. Crystal

representation and band and phonon band structures of  $\text{Ca}_2\text{SnO}_4$  (a),  $\text{Mg}_3\text{CdO}_4$  (b) and  $\text{MgSc}_2\text{O}_4$  (c).

## Discussion

---

We introduced a framework employing the denoising diffusion probabilistic model (DDPM) and point cloud representation for crystal structure generation. This versatile framework enables the generation of crystal structures composed of fewer than three elements and featuring up to 16 atom sites by specifying the elemental composition. To assess the framework's validity, we successfully reconstructed a batch of structures randomly sampled from the training dataset, affirming its reliability. Furthermore, we applied this framework to generate a batch of structures comprising rare earth elements, alkaline earth elements, transition metal elements and oxygen as an illustrative example. A total of 62.68% of the 746 structures had an  $E_{\text{hull}}/\text{atom}$  per atom less than 0.25 eV/atom, and 16.35% had an  $E_{\text{hull}}/\text{atom}$  per atom less than 80 meV/atom. In addition, several structures exhibited nonzero bandgaps, and their stability was confirmed through phonon spectrum analysis (e.g.,  $\text{Ca}_2\text{SnO}_4$ ,  $\text{Mg}_3\text{CdO}_4$ , and  $\text{MgSc}_2\text{O}_4$ ). Consequently, we demonstrated the efficacy of utilizing DDPM and point cloud representations in crystal structure generation, which was validated by DFT high-throughput calculations. This model serves as a foundational step, offering potential for further enhancement and the development of larger models for inverse crystal design. Furthermore, this approach serves to expand the database of crystals.

## Methods

---

At the core of our approach is the utilization of a diffusion model as the foundational model,

as illustrated in Fig. 5. We leverage U-Net<sup>32</sup> as the backbone of PCCD, a well-established architecture frequently employed for tasks such as classification and segmentation tasks<sup>33, 34</sup>.

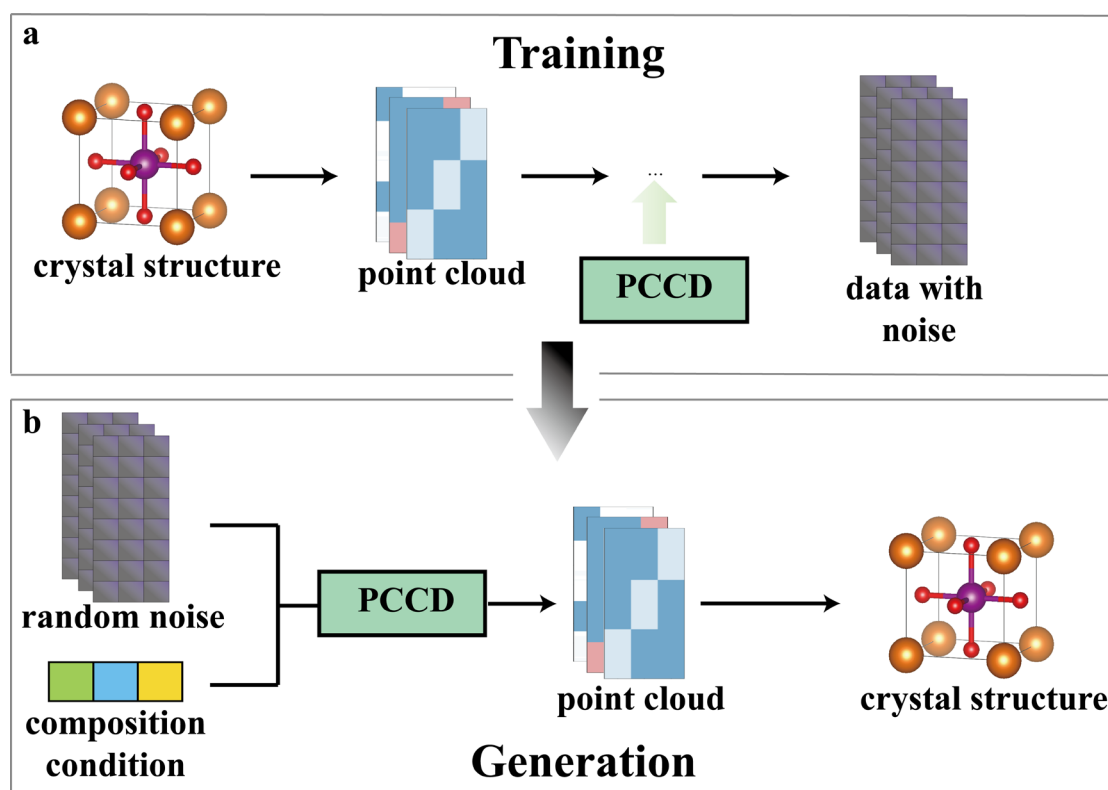


**Fig. 5|Sketch map of the PCCD. Here, we highlight the data flow of the framework. a.** Training phase process with data manipulation section. First, crystals are transformed to a point cloud data type, followed by the addition of noise to the data, which enables the PCCD to perform observation and learning; **b.** Generation phase with retrieval data operation. The method starts by feeding the PCCD random data and composition conditions and then passes to the data extraction and finishing with generating structures.

Two main methods are commonly used to represent a 3D object: voxels and point clouds. Voxel-based representation is thorough but resource intensive. In contrast, point clouds are more efficient than sparse matrices and reduce resource usage. Some prior works have claimed to use point clouds<sup>7</sup>, but they essentially used individual points to lower computational costs.

Our approach treats point clouds and lattice constants as three-channel entities akin to RGB in the computer vision (CV) field. We then employ clustering to determine the position, element composition and lattice.

Drawing from the notable achievements of diffusion models in the field of computer vision, we are motivated to extend their application to the generation of crystal structures. In this paradigm, we envision each crystal structure as akin to a patch in an image. To explore this innovative approach further, we integrate the point cloud representation technique with the power of diffusion models within the PCCD. This fusion of methods is designed to leverage the inherent advantages of both approaches. The diffusion model, renowned for its ability to capture intricate dependencies in data, holds promise for encoding the structural nuances of crystal formations. Moreover, the use of point cloud data representation, akin to a cloud of 3D points, serves to describe atomic positions and their attributes efficiently. By combining these two methodologies, we seek to harness their collective potential to revolutionize the generation and understanding of crystal structures.

## DATA PREPROCESSING

Our material data were sourced from the Materials Project (MP)<sup>2</sup>. In this extensive database, our selection process targeted structures with ternary, binary, or monadic compositions that feature a maximum of 16 atom sites. This thorough filtering yielded a comprehensive dataset comprising 52,028 distinct materials. This dataset encompasses a wealth of information, including the POSCAR file, band gap, magnetism, crystal system, magnetic ordering, etc., for each of these structures. However, for model efficiency, we opted to narrow

our focus to the band gap and magnetic ordering as the primary control variables. This decision, in conjunction with our use of the POSCAR files as training data, was made to streamline and lighten the model while ensuring the retention of essential variables for our specific research objectives.

As mentioned previously, we initially gathered various properties and POSCAR files of each crystal before training. The primary objective revolves around transforming the POSCAR data into a three-channel format, encompassing atom positions, element information, and lattice constants, as illustrated in Fig. 6. Each of these channels comprises 128 items, effectively representing each structure as a  $3 \times 128 \times 3$  ( $C \times W \times H$ ) matrix. The first channel is dedicated to atomic site information, where we distribute 128 points within the space. It is essential to clarify that the positions here are relative coordinates akin to those in the POSCAR file. The lattice vectors have not been determined at this stage. In essence, we use 128 items or several sets of data at this point in the process. To determine the absolute positions of these points, it is necessary to multiply them by the three lattice vectors obtained after processing the third channel. The data in the second channel correspond one-to-one with those in the first channel. Prior to generating or training samples, we input up to three elements. Each item in this channel contains three data values, which represent the likelihood of these three elements being associated with each atom. The data in the third channel do not correspond one-to-one with those in the first two channels. In fact, we want to obtain only six parameters  $\alpha, \beta, \gamma, a, b, c$  from here, which can be converted to three vectors. To match the shape before, we expand them to 128 items by copying. In theory, after training, two distinct groups of data are generated. We can then obtain three vectors by employing clustering techniques, determining the means of

each group, and performing calculations.

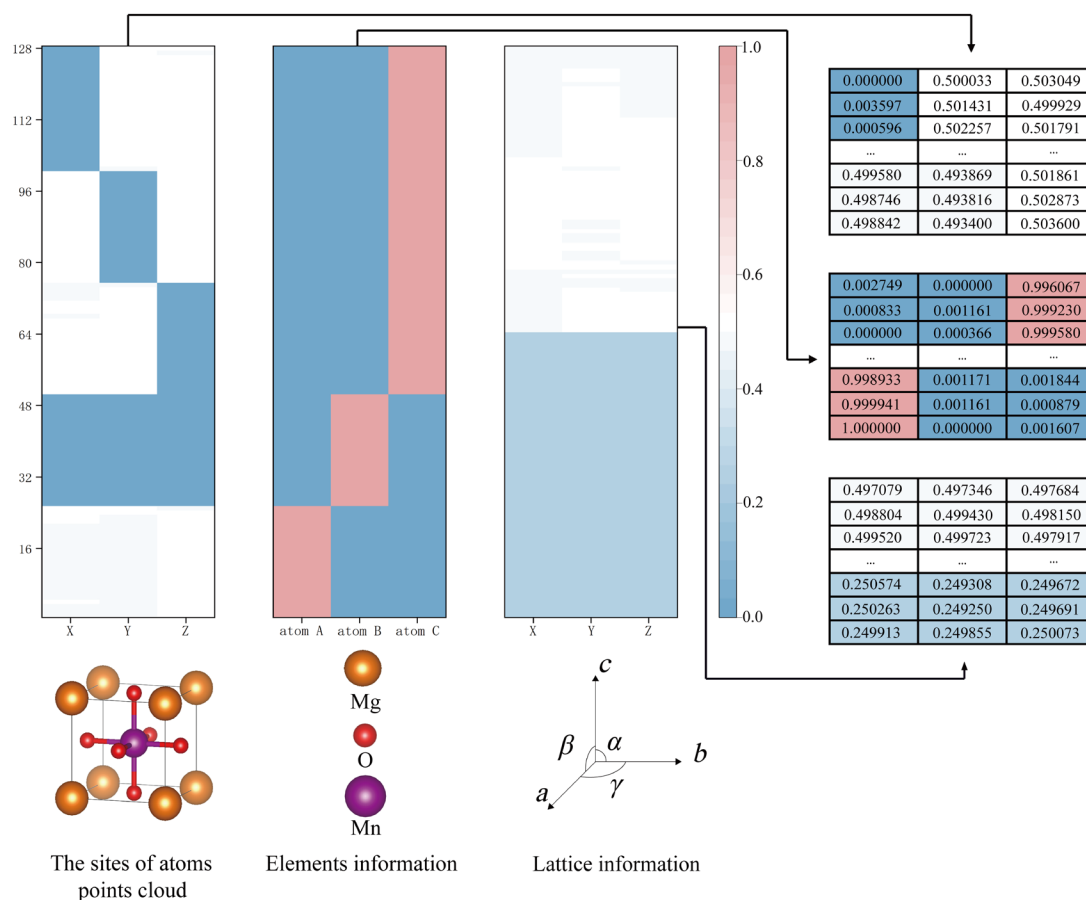


**Fig. 6|Data format for the framework (e.g., MgMnO<sub>3</sub>).** The first channel represents the position, the second channel represents the element information, and the third channel determines the lattice constants.

## GENERATION MODEL

Our generation model is based on the diffusion model, which is essentially a parameterized Markov chain. It is trained using variational inference to produce samples that closely match the data distribution after finite time<sup>18</sup>.

The diffusion model comprises two distinct processes, the training process and the generation process, often referred to as the sampling process, as illustrated in Fig. 7a. These



processes work in tandem to enable the generation of data samples that align with the underlying distribution of the training data. The training process can be briefly described as a procedure in which noise is progressively introduced to the data and the model endeavors to meet the characteristics of this noise addition. In contrast, the sampling process involves the gradual application of the trained model to denoise pure noise data. These data, in essence, are treated as source data with superimposed noise, and the model works to refine and clarify them.

The training process begins with  $x_0$  and gradually adds noise  $\epsilon_1, \epsilon_2, \dots, \epsilon_{T-1}, \epsilon_T$  to  $x_0$ , resulting in  $x_1, x_2, \dots, x_{T-1}, x_T$ . Assuming that  $x_0 \sim q(x_0)$  and the noise  $\epsilon_t$  follow a normal distribution, then, for  $t \geq 1$ :

$$q(x_{1:T}|x_0) = \prod_{t=1}^T q(x_t|x_{t-1}) \quad q(x_t|x_{t-1}) = \mathcal{N}(x_t; \sqrt{1 - \beta_t}x_{t-1}, \beta_t \mathbf{I}) \quad (1)$$

We follow the definition of J. Ho *et al.*<sup>18</sup> Here, we define a constant variance schedule  $\beta_1, \dots, \beta_T$ , where  $\beta$  increases as  $t$  increases. According to reparameterization, equation (1) can also be expressed as:

$$x_t = \sqrt{1 - \beta_t}x_{t-1} + \sqrt{\beta_t} \epsilon \quad (2)$$

where  $\epsilon \sim \mathcal{N}(0,1)$ . We can obtain  $x_t$  through the probability method from  $x_{t-1}$ . For simplicity, we define  $\alpha_t = 1 - \beta_t$ ,  $\bar{\alpha}_t = \prod_{s=1}^t \alpha_s$  and  $\bar{\beta}_t = \prod_{s=1}^t \beta_s$ . By applying equation (2) recursively, we can obtain that at any time  $t$ :

$$x_t = \sqrt{\bar{\alpha}_t}x_0 + \sqrt{1 - \bar{\alpha}_t}\epsilon, \quad q(x_t|x_0) = \mathcal{N}(x_0; \sqrt{\bar{\alpha}_t}x_0, (1 - \bar{\alpha}_t)\mathbf{I}) \quad (3)$$

and the reverse process begins with  $p(x_T) = \mathcal{N}(x_T, \mathbf{0}, \mathbf{I})$ ; this process denoises gradually as

$p_\theta(x_0) = \int p_\theta(x_{0:T}) dx_{1:T}$ . In the reverse process  $p_\theta$ , we know the variance of every step but do not know the means  $\mu_\theta$ .

$$p_\theta(x_{0:T}) = p(x_T) \prod_{t=1}^T p_\theta(x_{t-1}|x_t) \quad p_\theta(x_t|x_{t-1}) = \mathcal{N}(x_t; \mu_\theta(x_t, t), \beta_t I) \quad (4)$$

Therefore, we need to know what  $\mu_\theta$  is. It can be derived that<sup>18, 35</sup>:

$$\mu_\theta(x_t, t) = \frac{1}{\sqrt{\alpha_t}} \left( x_t - \frac{\beta_t}{\sqrt{1 - \bar{\alpha}_t}} \epsilon_\theta(x_t, t) \right) \quad (5)$$

After the parameterization (5), for any  $t \in [1, T]$ :

$$x_{t-1} = \frac{1}{\sqrt{\alpha_t}} \left( x_t - \frac{\beta_t}{\sqrt{1 - \bar{\alpha}_t}} \epsilon_\theta(x_t, t) \right) + \sigma_t z \quad (6)$$

$\epsilon_\theta$  is the model that needs to be trained. This means that we can obtain  $x_{t-1}$  from  $x_t$  by  $\epsilon_\theta$ .

In a one-step noise addition process (Fig. 7.b①), the noise is composed of random numbers following a normal distribution. The mean and variance of this noise depend on time  $t$  and the preceding data  $x_{(t-1)}$ . Simultaneously, the PCCD actively learns the characteristics of this noise. During each iteration, the model receives data with noise, and its primary task is to predict the most recent noise addition. Consequently, we end up with two types of noise: one generated from a probabilistic approach and the other predicted by our deep learning model. By comparing these two noise sources, we can calculate a loss, which serves as feedback to the model, facilitating its adjustment and improvement. This iterative process continues until the model effectively learns to reproduce the noise characteristics, achieving accurate denoising.

In the noise-removal process, as shown in Fig. 7b②, we only have data with noise, and

our objective is to estimate and separate the noise from the data. In this way, we can separate the current noise and the previous data. At the macro level, this is a disorderly to orderly process.

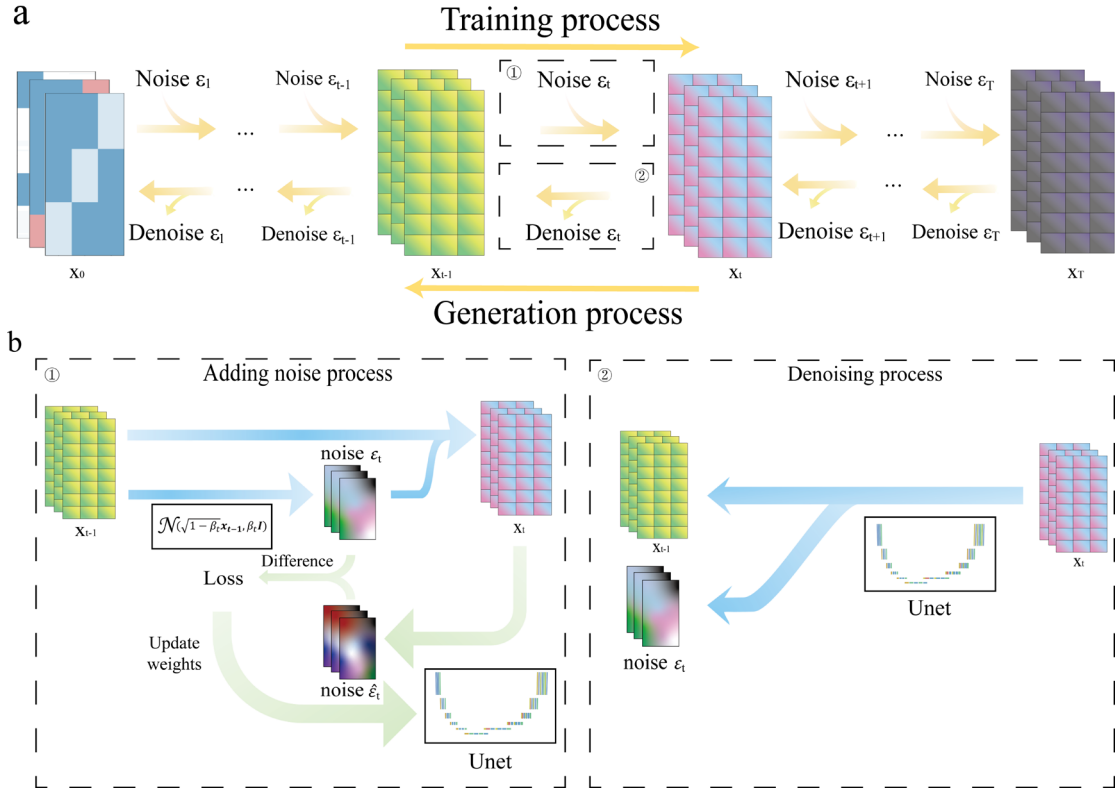


**Fig. 7|Schematic depiction of the PCCD architecture with generation and training processes. a.** The data flow of the training process and generation process. **b①.** A step of the training process of the model corresponds to part ① in a. **b②.** A step of the denoising process corresponds to part ② in a.

In this context, we employ a U-Net model (Supplementary Fig. 3) to predict and separate noise from the data. U-Net, initially introduced in 2015<sup>32</sup>, is a well-established model in the CV field that was notably acclaimed for its exceptional performance in image segmentation tasks. Our U-Net model is configured with five sets of upsampling and downsampling layers. To enhance its capacity to capture intrinsic data correlations, we incorporated intra-data correlation. This augmentation allows the model to effectively learn and predict noise, contributing to the

denoising process.

## Data availability

---

The crystal datasets used and analyzed during the current study are available in the *Materials Project* (<https://next-gen.materialsproject.org/>). Relevant data that support the key findings of this study are available within the article, the Supplementary Information and the `structure.csv` file. All raw data generated in the current study are available from the corresponding author upon request.

## Code availability

---

The code for this PCCD is available at <https://github.com/lzhelin/CrystalDiffusion> and <https://zenodo.org/records/10570395>

## Acknowledgements

---

This work gratefully acknowledges the financial support of the funding No. 4111190003 from Jiangsu University (JSU) and the National Natural Science Foundation of China (No. 11904137, 12074150 and 12174157). We gratefully acknowledge HZWTECH for providing computation facilities.

## References

---

1. Wang Y, Lv J, Zhu L, Ma Y. CALYPSO: A method for crystal structure prediction. *Computer Physics Communications* **183**, 2063-2070 (2012).
2. Jain A, *et al.* Commentary: The Materials Project: A materials genome approach to accelerating materials innovation. *APL Materials* **1**, (2013).
3. Pyzer-Knapp EO, Suh C, Gómez-Bombarelli R, Aguilera-Iparraguirre J, Aspuru-Guzik A. What Is High-Throughput Virtual Screening? A Perspective from Organic Materials Discovery. *Annual Review of Materials Research* **45**, 195-216 (2015).
4. Zhao Y, *et al.* Physics guided deep learning for generative design of crystal materials with symmetry constraints. *npj Computational Materials* **9**, 38 (2023).

5. Ren Z, *et al.* An invertible crystallographic representation for general inverse design of inorganic crystals with targeted properties. *Matter* **5**, 314-335 (2022).
6. Xie T, Fu X, Ganea O-E, Barzilay R, Jaakkola T. Crystal Diffusion Variational Autoencoder for Periodic Material Generation. Preprint at <https://ui.adsabs.harvard.edu/abs/2021arXiv211006197X> (2021).
7. Kim S, Noh J, Gu GH, Aspuru-Guzik A, Jung Y. Generative Adversarial Networks for Crystal Structure Prediction. *ACS Central Science* **6**, 1412-1420 (2020).
8. Kim B, Lee S, Kim J. Inverse design of porous materials using artificial neural networks. *Science Advances* **6**, eaax9324 (2020).
9. Sanchez-Lengeling B, Aspuru-Guzik A. Inverse molecular design using machine learning: Generative models for matter engineering. *Science* **361**, 360-365 (2018).
10. Merchant A, Batzner S, Schoenholz SS, Aykol M, Cheon G, Cubuk ED. Scaling deep learning for materials discovery. *Nature* **624**, 80-85 (2023).
11. Xie T, Grossman JC. Crystal Graph Convolutional Neural Networks for an Accurate and Interpretable Prediction of Material Properties. *Physical Review Letters* **120**, 145301 (2018).
12. Liu Y, Zhao T, Yang G, Ju W, Shi S. The onset temperature (T<sub>g</sub>) of As Se<sub>1</sub> glasses transition prediction: A comparison of topological and regression analysis methods. *Computational Materials Science* **140**, 315-321 (2017).
13. Fernandez M, Boyd PG, Daff TD, Aghaji MZ, Woo TK. Rapid and Accurate Machine Learning Recognition of High Performing Metal Organic Frameworks for CO<sub>2</sub> Capture. *The Journal of Physical Chemistry Letters* **5**, 3056-3060 (2014).
14. Goodfellow I, *et al.* Generative Adversarial Nets. In: *Neural Information Processing Systems* (2014).
15. Kingma DP, Welling M. Auto-Encoding Variational Bayes. Preprint at <https://ui.adsabs.harvard.edu/abs/2013arXiv1312.6114K> (2013).
16. Hoffmann J, Maestrati L, Sawada Y, Tang J, Sellier JM, Bengio Y. Data-Driven Approach to Encoding and Decoding 3-D Crystal Structures. Preprint at <https://ui.adsabs.harvard.edu/abs/2019arXiv190900949H> (2019).
17. Cao Y, *et al.* A Comprehensive Survey of AI-Generated Content (AIGC): A History of Generative AI from GAN to ChatGPT. Preprint at <https://ui.adsabs.harvard.edu/abs/2023arXiv230304226C> (2023).

18. Ho J, Jain A, Abbeel P. Denoising Diffusion Probabilistic Models. Preprint at <https://ui.adsabs.harvard.edu/abs/2020arXiv200611239H> (2020).
19. Ramesh A, Dhariwal P, Nichol A, Chu C, Chen M. Hierarchical Text-Conditional Image Generation with CLIP Latents. Preprint at <https://ui.adsabs.harvard.edu/abs/2022arXiv220406125R> (2022).
20. Nichol A, Jun H, Dhariwal P, Mishkin P, Chen M. Point-E: A System for Generating 3D Point Clouds from Complex Prompts. Preprint at <https://ui.adsabs.harvard.edu/abs/2022arXiv221208751N> (2022).
21. Balaji Y, *et al.* eDiff-I: Text-to-Image Diffusion Models with an Ensemble of Expert Denoisers. Preprint at <https://ui.adsabs.harvard.edu/abs/2022arXiv221101324B> (2022).
22. Kavar B, *et al.* Imagic: Text-Based Real Image Editing with Diffusion Models. Preprint at <https://ui.adsabs.harvard.edu/abs/2022arXiv221009276K> (2022).
23. Yang L, *et al.* Diffusion Models: A Comprehensive Survey of Methods and Applications. Preprint at <https://ui.adsabs.harvard.edu/abs/2022arXiv220900796Y> (2022).
24. Ebrahimi T, Alexiou E. On the performance of metrics to predict quality in point cloud representations. *Society of Photo-Optical Instrumentation Engineers (SPIE) Conference Series*, (2017).
25. Noh J, Kim J, Stein HS, Sanchez-Lengeling B, Jung Y. Inverse Design of Solid-State Materials via a Continuous Representation. *Matter* **1**, (2019).
26. Kresse GFJ. EFFICIENT ITERATIVE SCHEMES FOR AB INITIO TOTAL-ENERGY CALCULATIONS USING A PLANE-WAVE BASIS SET. *Physical Review, B Condensed Matter* **54**, (1996).
27. Kresse G. Ab initio molecular dynamics for liquid metals. *Journal of Non-Crystalline Solids* **192-193**, 222-229 (1995).
28. Kresse G, Joubert D. From ultrasoft pseudopotentials to the projector augmented-wave method. *Physical Review B* **59**, 1758-1775 (1999).
29. Perdew JP, Burke K, Ernzerhof M. Generalized Gradient Approximation Made Simple. *Physical Review Letters* **77**, 3865-3868 (1996).
30. Ong SP, Richards WD, Jain A, Hautier G, Ceder G. Python Materials Genomics (pymatgen): A robust, open-source python library for materials analysis. *Computational Materials Science* **68**, 314-319 (2013).

31. Blöchl PE. Projector augmented-wave method. *Physical Review B* **50**, 17953-17979 (1994).
32. Ronneberger O, Fischer P, Brox T. U-Net: Convolutional Networks for Biomedical Image Segmentation. Preprint at <https://ui.adsabs.harvard.edu/abs/2015arXiv150504597R> (2015).
33. Cho S-J, Ji S-W, Hong J-P, Jung S-W, Ko S-J. Rethinking Coarse-to-Fine Approach in Single Image Deblurring. Preprint at <https://ui.adsabs.harvard.edu/abs/2021arXiv210805054C> (2021).
34. Franani AO. Analysis of the performance of U-Net neural networks for the segmentation of living cells. *arXiv e-prints*, (2022).
35. Luo C. Understanding Diffusion Models: A Unified Perspective. Preprint at <https://ui.adsabs.harvard.edu/abs/2022arXiv220811970L> (2022).